Analysis and simulation of the multiple resistive switching modes occurring in HfO$_X$-based resistive random access memories using memdiodes

S. Petzold, E. Miranda, S. U. Sharath, J. Muñoz-Gorriz, T. Vogel, E. Piros, N. Kaiser, R. Eilhardt, A. Zintler, L. Molina-Luna, J. Suñé, and L. Alff

View Online   Export Citation   CrossMark

ARTICLES YOU MAY BE INTERESTED IN

Analysis and simulation of the multiple resistive switching modes occurring in HfO$_x$-based resistive random access memories using memdiodes

View Online   Export Citation   CrossMark

S. Petzold,[1,a] E. Miranda,[2] S. U. Sharath,[1] J. Muñoz-Gorriz,[2] T. Vogel,[1] E. Piros,[1] N. Kaiser,[1] R. Eilhardt,[1] A. Zintler,[1] L. Molina-Luna,[1] J. Suñé,[2] and L. Alff[1]

AFFILIATIONS

[1]Institute of Materials Science, Technische Universität Darmstadt, Alarich-Weiss-Straße 2, 64287 Darmstadt, Germany
[2]Departament d'Enginyeria Electrònica, Universitat Autònoma de Barcelona, 08193 Cerdanyola del Valles, Spain

[a]Author to whom correspondence should be addressed: petzold@oxide.tu-darmstadt.de

ABSTRACT

In this work, analysis and simulation of all experimentally observed switching modes in hafnium oxide based resistive random access memories are carried out using a simplified electrical conduction model. To achieve switching mode variation, two metal-insulator-metal cells with identical stack combination, but varying oxygen stoichiometry of the hafnia layer, namely, stoichiometric vs highly deficient, are considered. To access the individual switching modes, the devices were subjected to a variety of cycling conditions comprising different voltage and current ranges. For modeling the device behavior, a single or two antiserially connected memdiodes (diode with memory) were utilized. In this way, successful compact simulation of unipolar, bipolar, threshold, and complementary resistive switching modes is accomplished confirming the coexistence of two switching mechanisms of opposite polarity as the basis for all observable switching phenomena in this material. We show that only calibration of the outer current–voltage loops with the memdiode model is necessary for predicting the device behavior in the defined region revealing additional information on the switching process. The correspondence of each memdiode device with the conduction characteristics of the individual top and bottom metal-oxide contacts allows one to assess the role played by each interface in the switching process separately. This identification paves the path for a future improvement of the device performance and functionality by means of appropriate interface engineering.

I. INTRODUCTION

Resistive random access memories (RRAMs) have been intensively studied during the last decade revealing promising characteristics such as fast switching speed in the subnanosecond region,[1] low voltage operation, low power consumption,[2] resilience toward ionizing radiation,[3] and scalability[4] below 10 nm. Consisting of a simple metal-insulator-metal (MIM) structure and being manufacturable with complementary metal-oxide-semiconductor (CMOS) compatible materials, e.g., hafnium or tantalum oxide makes RRAM back-end-of-line (BEOL) compatible and, thus, an interesting candidate for applications in the Internet of Things[5] (IoT) fostering the so-called "More than Moore"[6] approach. In general, RRAM enables storage densities as small as 4F^2 and 4F^2/n through 3D stacking.[7] Moreover, RRAM is investigated within the scope of in-memory computing and is believed to be a suitable candidate for multibit operations, thanks to its multilevel storage capability. The plasticity exhibited by RRAM cells also enables mimicking neuronal networks[8,9] with the RRAM cell acting as the electrical synapse,[10] highlighting its role in applications such as image recognition and autonomous driving. Although extensively investigated and already introduced in the market[11] as early as in 2013, the underlying switching mechanisms of valence change memory (VCM) cells are not completely understood. The switching process relies on the formation (forming/set) and dissolution (reset) of a metal-rich atom-sized pathway pictured as a conductive filament (CF). The filament formation requires an initial activation voltage that leads to a redistribution of oxygen atoms which results in an increased local density of oxygen vacancies in the dielectric layer, thus creating a defect

band which enables local current transport through the dielectric. By applying an appropriate voltage protocol, part of the previously removed oxygen is recaptured by the vacancy sites causing the rupture of the conductive filament thus increasing the resistance state of the device. In this way, the device can be reversibly switched from a high resistance state (HRS) to a low resistance state (LRS) and vice versa. A number of different factors, such as the oxygen affinity or roughness of the electrodes, the diffusion barriers for oxygen transport in the dielectric, or the high local current densities resulting in Joule heating up to 1000 K,[12] participate in or influence the switching mechanism making it a complex process hard to disentangle. Therefore, a clear picture and understanding of the conductive filament in VCM is still missing. Although indirect probing techniques, such as conductive atomic force microscopy, can be utilized to verify and locate conductive filaments,[13–15] it can only render limited information. Opposed to conductive bridge RAM, a direct imaging of the conductive filament via transmission electron microscopy is more complex since the filament is not based on nonhost cations (e.g., Cu), but on defects in the anion sublattice of the dielectric (oxygen vacancies). Although various approaches are being followed in order to gain further insight,[16–19] a clear atomistic picture with a correlation to the switching characteristics is still not finalized. Hence, every new finding about the characteristics of the conductive filament in the switching process, which further improves the understanding of the resistive switching process, is important.

So far, four different switching modes have been identified in the literature, namely, bipolar resistive switching (BRS), unipolar resistive switching (URS), threshold resistive switching (TRS), and complementary resistive switching (CRS). While the first two can be categorized as nonvolatile, i.e., memory type, the latter two can also be utilized for the volatile selector-type switching mechanisms. The BRS mode can be additionally differentiated to figure eight-wise (f8) and counter figure eight-wise (cf8) switching depending on the voltage polarity of the switching loop. In this study, a simplified behavioral model that clarifies how BRS-f8 and BRS-cf8, as well as CRS, can coexist in the same device and be transmuted into each other is reported. Within the proposed framework, the prerequisites necessary for observing both URS and TRS, which can be represented by the same approach and also transmuted to BRS under certain conditions, are also discussed.

II. EXPERIMENTAL AND OXYGEN ENGINEERING

The stacks used in this work ($TiN/HfO_2/Pt$ and $TiN/HfO_{1.5}/Pt$) were grown using a custom designed molecular beam epitaxy (MBE) unit enabling the tuning of the oxygen content (crystal structure) of the functional hafnia layer in the full range from metallic hafnium to highly deficient (tetragonal) to stoichiometric (monoclinic) films. The oxygen content of the dielectric layer was controlled via the oxygen flow rate and radio frequency power of the radical source. For CMOS compatibility and for stabilization of the tetragonal and monoclinic phases of the 20 nm thick hafnia layer, a growth temperature of 320 °C was chosen. The two-theta X-ray diffraction patterns for the predominantly tetragonal and monoclinic hafnia stacks are depicted in Fig. 1(a). Further details about the oxide growth process and the quantitative evaluation of the oxygen stoichiometry can be found in Ref. 20. A schematic

overview of the investigated stack is depicted in Fig. 1(b) with bright-field transmission electron microscope images for the Si (100)-substrate, the magnetron sputtered titanium nitride electrode, and the tetragonal (left) and monoclinic (right) hafnia layers, respectively. The platinum top electrode (TE) was deposited *ex situ* by magnetron sputtering. Therefore, the depicted Pt electrode is only a schematic representation of the actual polycrystalline platinum electrode. For the tetragonal hafnia layer ($HfO_{1.5}$), the crystal size was found to be smaller and the interface to TiN was found to be distinct compared to the monoclinic (HfO_2) hafnia layer. The impact of the oxygen content of the dielectric layer on the electronic structure can be seen by the low-loss electron energy-loss spectra depicted in Fig. 1(c), which shows a clear difference between deficient and stoichiometric films. The electronic structure fingerprints of stoichiometric m-HfO_2 and oxygen deficient t-$HfO_{1.5}$ are in agreement with the literature.[20,21] The electron energy loss near edge structure (ELNES) features in the spectra are denoted as α to η, which correspond to A to H in Ref. 21. The change in the electronic structure of the hafnia layer also affects the optical bandgap of the material. In Fig. 1(d), the UV/Vis-absorption spectra of a deficient and stoichiometric amorphous hafnia reference sample are depicted. By evaluating energy vs α^2 plots, the bandgap of deficient hafnia is found to reduce by
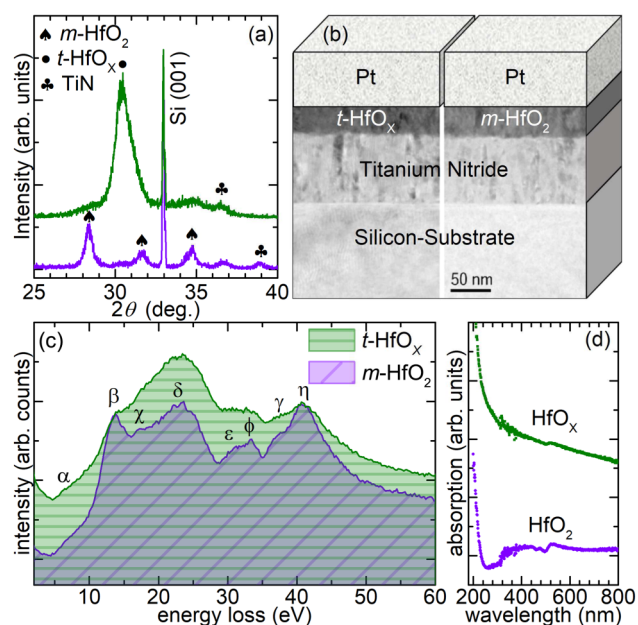

FIG. 1. (a) X-ray diffraction pattern for the investigated stack consisting of tetragonal (green) and monoclinic (purple) hafnium oxide. (b) Overview of the Si/TiN/hafnia/Pt-stacks with stoichiometric HfO_2 or oxygen deficient $HfO_{1.5}$, respectively. For silicon, TiN and Hafnia, representative TEM bright-field images are depicted. (c) Electron energy-loss spectra for m-HfO_2 and t-$HfO_{1.5}$, respectively, displaying their difference in electronic structure. (d) UV/Vis-absorption spectra of amorphous, deficient, and stoichiometric hafnia reference samples. The optical bandgap reduces by 0.5 eV from stoichiometric (5.7 eV) to deficient (5.2 eV) hafnia.

0.5 eV compared to the stoichiometric hafnia layer resulting in optical bandgaps of 5.2 and 5.7 eV, respectively. In this work, the resistive switching behavior of highly deficient hafnia devices ($HfO_{1.5}$) to fully oxidized, stoichiometric hafnia devices (HfO_2) of 20 nm film thickness was investigated and compared. The electrical characterization was performed using a Keithley Semiconductor Characterization System 4200 (SCS 4200) by applying bias to the platinum top electrode (TE) while grounding the titanium nitride back electrode (BE).

III. MEMDIODE MODEL

The compact model considered here to deal with the different conduction modes exhibited by our devices consists of a single memdiode structure, i.e., a diode with hysteretic properties, or in a combination of memdiodes. The memdiode model was originally presented in Ref. 22 and later extended in Ref. 23. For the sake of completeness, here it is succinctly reviewed. Physically, the memdiode represents the presence of a potential barrier that controls the electron flow. The conduction properties of this nonlinear device change according to the variation of this barrier. Because of the uncertainty in the area of the CF, instead of the potential barrier height, the current amplitude is used as the reference variable. Following a memristive approach, the proposed model relies on two equations, one for the electron transport expressed as a diode with a series resistance and a second equation for the memory state of the device which is based on a hysteresis operator. The equation for the I–V characteristic of a single memdiode M is given by

$$I = \text{sgn}(V)\{(\alpha R)^{-1} W\{\alpha R I_0(\lambda) \exp[\alpha(\text{abs}(V) + R I_0(\lambda))]\} - I_0(\lambda)\}, \quad (1)$$

where $I_0(\lambda) = I_{\min}(1 - \lambda) + I_{\max}\lambda$ is the diode current amplitude, α is a constant related to the particular features of the conduction mechanism, and R is a series resistance. Equation (1) is the solution of a diode with series resistance and W is the Lambert function. $I_{\min}$ and $I_{\max}$ are the minimum and maximum values of the current amplitude, respectively. $\text{abs}(V)$ is the absolute value of the applied bias, and sgn is the sign function. As I_0 increases in (1), the I–V curve changes its shape from exponential to linear as experimentally observed for this kind of devices. λ is a control parameter that runs between 0 and 1 and is given by the recursive operator,

$$\lambda(V) = \min\left\{\Gamma^-(V), \max\left[\lambda\left(\overleftarrow{V}\right), \Gamma^+(V)\right]\right\}, \quad (2)$$

where min and max are the minimum and maximum functions, respectively. The positive and negative ridge functions in (2) are defined as

$$\Gamma^+(V) = \{1 + \exp[-\eta^+(V - V^+)]\}^{-1} \quad (3)$$

and

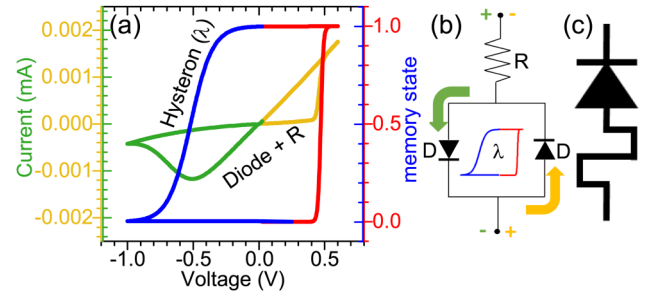$$\Gamma^-(V) = \{1 + \exp[-\eta^-(V - V^-)]\}^{-1}. \quad (4)$$

FIG. 2. (a) Typical current–voltage characteristic and memory state loop associated with the memdiode model. In this case, the transition rates are different for positive and negative voltages. (b) Equivalent circuit model for the current equation (1). R is the series resistance. The diodes are driven by the memory state of the device and one diode D is activated at a time. For (a) and (b), the green curve represents current in neg. voltage direction (yellow—positive voltage bias). (c) Electrical symbol for the memdiode.

Equations (3) and (4) represent the transition from HRS to LRS and vice versa and can be physically connected with the completion and destruction of the CF,[22] respectively. η^+ and η^- are the transition rates, and V^+ and V^- are the set and reset voltages. $\overleftarrow{V}$ is the voltage a time step before V. $\Gamma^+(V)$ and $\Gamma^-(V)$ define the so-called hysteron or memory map of the device which records the history of the device as a function of the applied voltage [see Fig. 2(a)]. The initial value λ_0 determines whether the device starts in LRS ($\lambda_0 = 1$) or HRS ($\lambda_0 = 0$). λ calculated from (2) yields the transition from HRS to LRS and vice versa through a change in the properties of the diodes depicted in Fig. 2(b). This λ is used in turn to compute the current given by (1). The final result is a current loop as that illustrated in Fig. 2(a). Notice that only one diode D within the memdiode is activated at the time depending on the applied bias polarity. Inverse currents are neglected. Additionally, time effects (pulsed measurements and ramp rate effects) are not considered for present purposes but can be included as well using the extended model reported in Ref. 23. The forward direction of the memdiode [see Fig. 2(c)] is defined so as to have positive V^+ and negative V^- [yellow and green curves in Fig. 2(a)]. As an example, the model parameters used in Fig. 3(a) for the BRS-cf8 curve are $I_{\min} = 5.0 \cdot 10^{-6}$ A, $I_{\max} = 5.5 \cdot 10^{-3}$ A, $\alpha = 2.1$ eV^{-1}, $R = 100\,\Omega$, $V^+ = -2.02$ V, $V^- = 0.7$ V, $\eta^+ = -100$ V^{-1}, $\eta^- = -5.2$ V^{-1}, and $\lambda_0 = 0$. For the BRS-f8 curve [Fig. 3(c)], the model parameters are $I_{\min} = 6.5 \cdot 10^{-5}$ A, $I_{\max} = 4.0 \cdot 10^{-3}$ A, $\alpha = 2.1$ eV^{-1}, $R = 250\,\Omega$, $V^+ = 0.47$ V, $V^- = -0.52$ V, $\eta^+ = 100$ V^{-1}, $\eta^- = 12$ V^{-1}, and $\lambda_0 = 0$. Notice that these electrical parameters can be connected to the physics through a proper choice of a particular conduction mechanism. It is worth mentioning that the model uses the outer I–V characteristic (major loop) as the calibration curve but can deal with arbitrary input signals (minor loops). The compliance is simply introduced as a limit in the current magnitude given by (1).

IV. RESULTS AND DISCUSSION

The experimental and simulated curves corresponding to the different switching modes detected in hafnia are summarized in Fig. 3. The red curves are simulations while the green and yellow
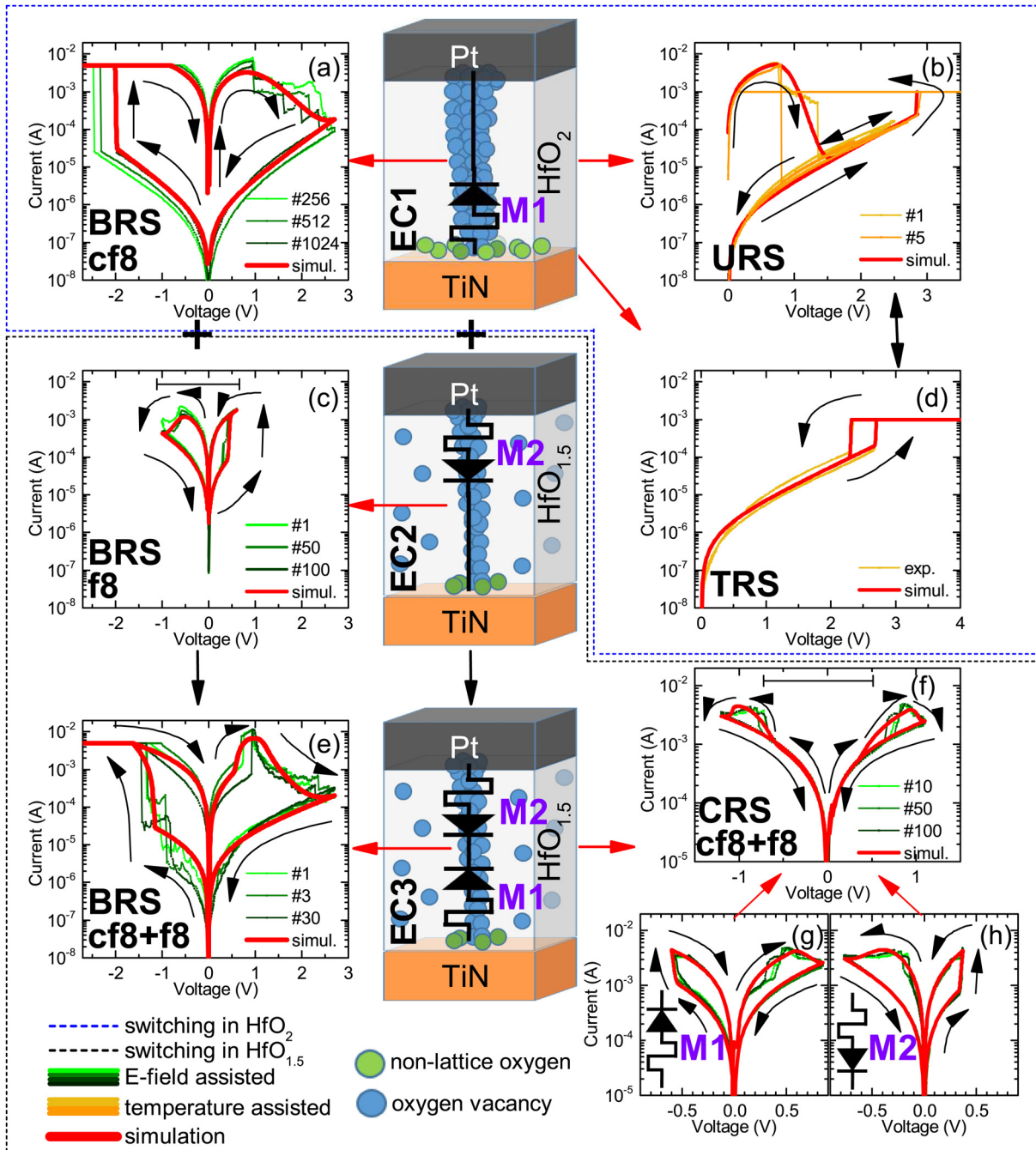
FIG. 3. The blue dotted box includes the resistive switching curves associated with the stoichiometric HfO_2-stack, while the black dotted box includes the curves of the deficient $HfO_{1.5}$-stack, respectively. The stacks in the center (EC1, 2, and 3) represent the equivalent circuits used for simulating the corresponding switching modes (indicated by red arrows); M1 and M2 represent two memdiodes of opposite voltage polarity; the switching curves are named as follows: (a) counter figure eight-wise bipolar resistive switching (cf8-BRS); (b) unipolar resistive switching (URS); (c) figure eight-wise bipolar resistive switching (f8-BRS); (d) threshold resistive switching (TRS); (e) superimposed counter figure and figure eight-wise bipolar resistive switching (cf8 + f8-BRS); (f) complementary resistive switching (CRS) also being a superposition of f8 and cf8-BRS; (g) and (h) extracted I–V curves for diodes M1 and M2 which when combined in series result in the CRS of (f). Greenish curves represent experimental curves of bipolar nature and, therefore, are indicated as E-field assisted, while the yellowish curves represent experimental curves of unipolar nature and, therefore, are indicated as temperature assisted, respectively. # indicates the depicted cycle number. The red curves always represent the simulated curves of the model.

lines are experimental data with # indicating the depicted cycle number. A thorough description of the complete set of experiments carried out can be found in Ref. 20. The plots inside the blue dotted box are switching modes observed for the stoichiometric (HfO$_2$) stack, namely, cf8-BRS [Fig. 3(a)], URS [Fig. 3(b)], and TRS [Fig. 3(d)]. The plots inside the black dotted box correspond to the switching curves for the highly deficient hafnia (HfO$_{1.5}$) stack, namely, f8-BRS [Fig. 3(c)], a combination of cf8- and f8-BRS [Fig. 3(e)], and CRS [Fig. 3(f)]. Altogether, the two considered stacks show all observed resistive switching modes reported in the literature for HfO$_x$, whereby only one material parameter was changed, namely, the initial oxygen vacancy concentration. We found that all switching modes associated with the stoichiometric sample can be simulated using a single memdiode as illustrated in the schematic EC1 in Fig. 3. Nevertheless, for the deficient stack an additional memdiode with opposite polarity (EC2 and EC3 in Fig. 3) is required for fitting the experimental curves. This distinction indicates that for the deficient stack case an additional switching phenomenon is superimposed to the observed cf8-BRS behavior corresponding to the stoichiometric stack, which was found to result in the observed CRS [Fig. 3(f)] and combined f8 + cf8-BRS [Fig. 3(e)], respectively. The switching mechanism associated with the opposite polarity is operating in a lower voltage regime and thus can be isolated by choosing the appropriate voltage program. This consideration results in the f8-BRS switching behavior shown in Fig. 3(c). EC2 also consists of two antiserially connected memdiodes, but since the voltage program has been reduced only M2 is activated, while M1 simply acts as a series resistor. If the voltage span is increased (from −2.7 to +2.7 V), the second memdiode comes into play affecting the I–V curve [see Fig. 3(e)] which qualitatively is the superimposed switching behavior depicted in Figs. 3(a) and 3(c), respectively, and also depicted in the equivalent circuit EC3 as the series combination of M1 and M2. Notice how the proposed model is able to capture the repetitive hump in the positive side of the I–V curve in Fig. 3(e). If the voltage protocol is further increased with respect to that shown in Fig. 3(c), the set event in the f8-switching is followed by the reset event in the cf8-switching for the positive voltage direction, while for the negative voltage direction the set event in the cf8-switching is followed by the reset event in the f8-switching thus resulting in the CRS mode [see Fig. 3(f)]. Therefore, all switching modes attributed to the deficient HfO$_{1.5}$-stack [Figs. 3(c), 3(e), and 3(f)] can be represented by two memdiodes in series as depicted in the schematic EC3. Model results for an arbitrary input signal (sinusoidal in this case) displaying the interplay of f8-set and cf8-reset resulting in the CRS are depicted in Fig. 4. In (a) and (b), voltage- and current vs time characteristics of the f8 + cf8 switching operation are depicted, respectively. Due to an appropriate calculation of the f8 + cf8 switching operation, any input signal within the calibration region is feasible and renders fitting output data. The input does not need to be linear. Figure 4(c) is the composition of (a) and (b). When the operation voltage is limited to 1.3 V, the CRS mode can be isolated within the f8- and cf8-BRS switching operation of the HfO$_{1.5}$ stack. Below 1 V, the set in the f8-operation dominates the device behavior resulting in a decrease of the overall device resistance being attributed to memdiode M2 (HfO$_x$|Pt). Beyond 1 V, the reset in cf8-operation is activated overall increasing the device
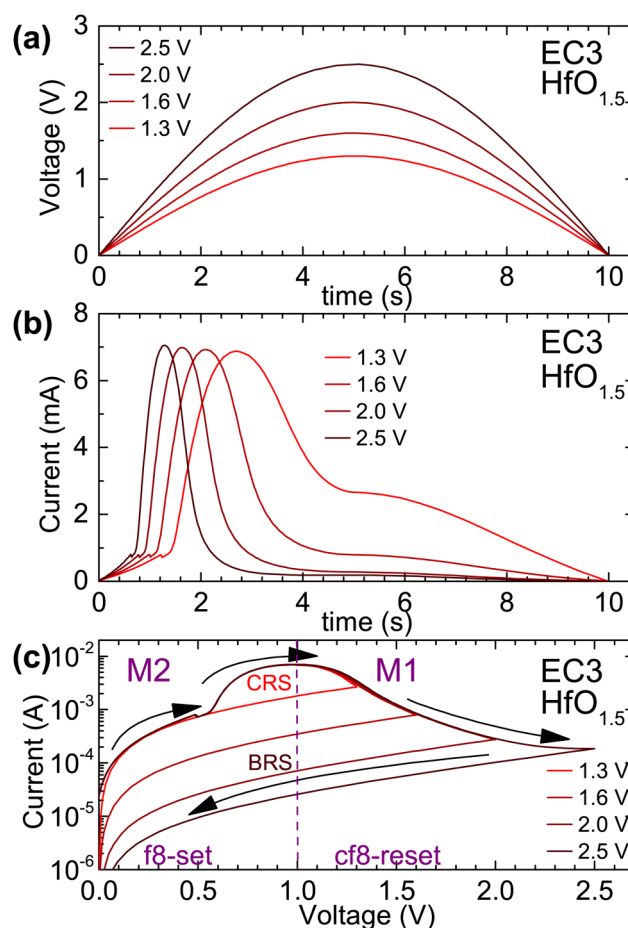

FIG. 4. Simulated switching behavior of the deficient HfO$_{1.5}$ stack in the positive voltage direction. (a) Applied voltage vs time, (b) current vs time, and (c) current vs voltage of the f8 + cf8 switching operation. Note that (c) is the composition of (a) and (b). By limiting the operation voltage to 1.3 V, the CRS can be isolated which is correlated to the set of the f8-switching (M2—Pt|HfO$_x$) followed by the reset of the cf8-operation (M1—TiN|HfO$_x$). By further increasing the operation voltage, the reset of the cf8-operation is driven forward further resetting the device to a higher resistance state.

resistance [M1 (TiN|HfO$_x$)]. By stopping the reset process at 1.3 V, CRS can be produced. By further increasing the operation voltage, the reset process of the cf8-operation can be carried on to higher resistance levels of the HRS resulting in the observed f8 + cf8 switching operation.

For the investigated stacks, the superimposed switching modes with opposite polarity can be attributed to the effects occurring at the two oxide interfaces, namely, Pt/HfO$_x$ and HfO$_x$/TiN. While TiN is able to form bonds to oxygen of ionic-covalent character forming titanium oxynitride[24] (TiON), and which has been suggested in the literature to participate in the switching process,[25] platinum is classified as an inert material showing catalytic properties. Therefore, the binding energy of oxygen at the Pt/HfO$_x$-interface is

considerably lower than for the TiN/HfO$_x$-interface.[26,27] The observed f8-switching is thus attributed to the electric field dominated storage and recapture of the mobile oxygen ions at the Pt-interface, occurring at lower operation voltages with opposite polarity (including lower on/off ratios) than the cf8-switching which we attribute to the interaction with the TiN-interface. As can be seen from Fig. 3, only for the deficient stack combination, the Pt-interface also actively participates in the switching process (M1 + M2), while for the stoichiometric stack only the TiN-interface is considered to be active in BRS (M1). This can be explained by the different oxygen content in the hafnia layers resulting in a different electroforming process, thus influencing the conductive filament. Due to the deficiency of oxygen by oxygen engineering[28,29] in the HfO$_{1.5}$-stack, the voltage used to electroform the device is found to be in the range of the operation voltages for set and reset, thus considered "forming-free." Due to the pre-existent oxygen deficiency, in principle, no further creation of oxygen vacancies—but rather a redistribution of oxygen in the dielectric layer is necessary for the formation of a conductive pathway resulting in a cylindrical-shaped filament (as schematically shown in Fig. 3, EC2 and EC3, respectively). Additionally, it was found that the f8-switching could be further stabilized by applying a two-step forming process, starting by a first forming step in the positive voltage direction (oxygen moving toward Pt), followed by a second step in the negative voltage direction (oxygen moving toward TiN). On the other hand, no pre-existent oxygen vacancies facilitate the switching process for the stoichiometric HfO$_2$-stack. This means that every oxygen vacancy needs to be created first, resulting in the storage of oxygen at the TiN-interface. In this case, a higher forming voltage of about −7 V is required, resulting in higher current overshoots, and in turn in stronger Joule heating effects, with a consequent more vigorous breakdown of the dielectric layer. This generates a less uniform conductive filament (likely conical-shaped) with a single active interface in the subsequent switching loops. As described above, the single or the two-memdiode model used for simulations is of wide range applicability. Here, we related the observed superimposed switching mechanisms to the different interfaces but the distinctive behavioral analysis can also be extended to other systems such as multilayer stacks, e.g., TiN/HfO$_2$/Hf/HfO$_2$/TiN which have been shown to exhibit CRS due to two antiserially connected resistor elements.[30]

For the stoichiometric HfO$_2$-stack, URS was also identified. While BRS operates in both voltage polarities, URS is detected only for positive bias. It has been reported in the literature[31] that URS and BRS are the result of different dominating physical processes which are for the case of BRS more E-field dominated and for the case of URS more dependent on thermal effects. Thermal effects can arise from the local temperature increase associated with the high current densities and high local electric fields within the filament or in the case of a ruptured filament with the virtual electrode emission. Thereby, instead of field driven migration of oxygen (as in the case of BRS), effects such as Fick's diffusion and Soret[31,32] forces dominate the oxygen transport accounting for ion transport along concentration and temperature gradients, respectively. In this case, oxygen displacements are likely to be more lateral within the dielectric layer rather than directed toward the electrodes. Still, this behavior can be modeled by solely making use of one memdiode with positive V^+ and V^-. The single memdiode

model also accounts for the occasionally observed TRS mode which coexists with the URS mode [see Fig. 3(d)]. TRS is ascribed to a thermal runaway process, e.g., insufficient heat dissipation,[33] resulting in the formation of an unstable filament.

Additional information on each memdiode (each interface behavior) can be easily extracted in the case of CRS since almost identical parameters for both opposite devices are considered. This is illustrated in Figs. 3(f)–3(h). In Figs. 3(g) and 3(h), the individual I–V curves for M1 and M2 are plotted. The combined result is shown in Fig. 3(f). In this case, model parameters for M1 are $I_{min} = 6.0 \cdot 10^{-4}$ A, $I_{max} = 9.0 \cdot 10^{-3}$ A, $\alpha = 2.2$ eV^{-1}, $R = 70\,\Omega$, $V^+ = 0.6$ V, $V^- = -0.6$ V, $\eta^+ = 100$ V^{-1}, $\eta^- = 15$ V^{-1}, and $\lambda_0 = 0$, while for M2: $I_{min} = 6.0 \cdot 10^{-4}$ A, $I_{max} = 7.0 \cdot 10^{-3}$ A, $\alpha = 2.2$ eV^{-1}, $R = 10\,\Omega$, $V^+ = 0.37$ V, $V^- = -0.4$ V, $\eta^+ = 100$ V^{-1}, $\eta^- = 10$ V^{-1}, and $\lambda_0 = 1$. Notice that the initial memory states for M1 and M2 are the opposite. Further insight into the role of interfaces within the resistive switching process can be achieved by analyzing the potential drops in each memdiode. A detailed analysis of one CRS switching cycle is depicted in Fig. 5. In Fig. 5(a), the green and red curves are the experimental and simulated current-time characteristics, respectively. The black curve in Fig. 5(b) corresponds to the applied triangular voltage sweep. The blue and cyan curves are the voltage drops across M1 (TiN|HfO$_x$) and M2 (Pt|HfO$_x$), respectively. Notice that the distribution of voltages is by no means intuitive. This kind of analysis is of utmost relevance since one can pinpoint the role of each interface in the switching process and, therefore, theoretically modify their properties for the appropriate target. The same
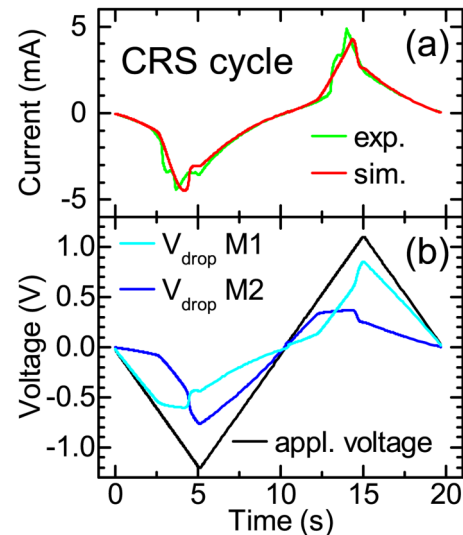

FIG. 5. (a) Current- and (b) voltage-time evolution within one switching cycle of the CRS mode [as depicted in Fig. 2(f)]. (a) The green curve is the experimental current evolution, while the red curve represents the simulated current through both memdiodes. (b) The black curve represents the applied voltage program starting at 0 V toward −1.2 V, followed by a linear voltage increase up to +1.2 V and down to 0 V. The cyan and blue curves are the corresponding voltage drops at the individual TiN|HfO$_x$ (M1) and Pt|HfO$_x$ (M2) interfaces (memdiodes), respectively.

procedure can be applied to the other cases investigated, but this requires more sophisticated algorithms for the model parameters extraction.

V. CONCLUSION

In summary, it was shown that all reported switching modes for VCM-type RRAMs, in particular, for HfO_x-based devices, can be closely described by a simplified electrical conduction model. To model all experimentally observed switching modes, the interface behavior was represented by one or two opposite-biased memdiodes in series with appropriate initial conditions. While URS, TRS, f8- and cf8-BRS can each be described by a single memdiode, the observed CRS is only accessible by choosing the optimal voltage region of the superimposed f8 + cf8-BRS and needs to be described by two memdiodes. The separation of effects occurring at both interfaces strongly supports the qualitative physical picture discussed in Ref. 20. Interestingly, the proposed approach can also be used to represent other stack combinations, for example, bilayer or multilayer stacks.[30,33] By modeling, we were able to extract information on the individual interfaces, such as the potential drop distribution (and, therefore, their resistance evolution), which can be used in the future for engineering and fine tuning the switching process of these devices. To further improve the demonstrated behavioral model, additional cycle to cycle variation, stepwise transitions, temperature effects, and pulse operation applicability could be implemented in future.

REFERENCES

[1] A. C. Torrezan, J. P. Strachan, G. Medeiros-Ribeiro, and R. S. Williams, "Sub-nanosecond switching of a tantalum oxide memristor," Nanotechnology **22**(48), 485203 (2011).

[2] C. H. Cheng, C. Y. Tsai, A. Chin, and F. S. Yeh, "High performance ultra-low energy RRAM with good retention and endurance," in *2010 IEEE International Electron Devices Meeting (IEDM)* (IEEE, 2010), pp. 19.4.1–19.4.4.

[3] S. Petzold, S. U. Sharath, J. Lemke, E. Hildebrandt, C. Trautmann, and L. Alff, "Heavy ion radiation effects on hafnium oxide based resistive random access memory," IEEE Trans. Nucl. Sci. 1-1 (2019), see https://ieeexplore.ieee.org/stamp/stamp.jsp?tp=&arnumber=8688490&tag=1.

[4] Z. Zhang, Y. Wu, H. S. P. Wong, and S. S. Wong, "Nanometer-scale HfO_x RRAM," IEEE Electron Device Lett. **34**(8), 1005–1007 (2013).

[5] D. Ielmini, "Resistive switching memories based on metal oxides: Mechanisms, reliability and scaling," Semicond. Sci. Technol. **31**(6), 063002 (2016).

[6] T. Hino, T. Hasegawa, K. Terabe, T. Tsuruoka, A. Nayak, T. Ohno, and M. Aono, "Atomic switches: Atomic-movement-controlled nanodevices for new types of computing," Sci. Technol. Adv. Mater. **12**(1), 013003 (2011).

[7] S. Yu, H. Y. Chen, B. Gao, J. Kang, and H. S. P. Wong, "HfO_x-based vertical resistive switching random access memory suitable for bit-cost-effective three-dimensional cross-point architecture," ACS Nano **7**(3), 2320–2325 (2013).

[8] M. Ziegler, C. Wenger, E. Chicca, and H. Kohlstedt, "Tutorial: Concepts for closely mimicking biological learning with memristive devices: Principles to emulate cellular forms of learning," J. Appl. Phys. **124**(15), 152003 (2018).

[9] G. Pedretti, V. Milo, S. Ambrogio, R. Carboni, S. Bianchi, A. Calderoni, and D. Ielmini, "Stochastic learning in neuromorphic hardware via spike timing dependent plasticity with RRAM synapses," IEEE J. Emerg. Sel. Top. Circuits Syst. **8**(1), 77–85 (2018).

[10] S. Petzold *et al.*, "Gradual reset and set characteristics in yttrium oxide based resistive random access memory," Semicond. Sci. Technol. **34**(7), 075008 (2019).

[11] M. Xiangchao *et al.*, "A 16 Mb RRAM test chip based on analog power system with tunable write pulses," in *2015 15th IEEE Non-Volatile Memory Technology Symposium (NVMTS)* (IEEE, 2015).

[12] E. Yalon, S. Cohen, A. Gavrilov, and D. Ritter, "Evaluation of the local temperature of conductive filaments in resistive switching materials," Nanotechnology **23**(46), 465201 (2012).

[13] U. Celano, L. Goux, A. Belmonte, K. Opsomer, A. Franquet, A. Schulze, C. Detavernier, O. Richard, H. Bender, M. Jurczak, and W. Vandervorst, "Three-dimensional observation of the conductive filament in nanoscaled resistive memory devices," Nano Lett. **14**(5), 2401–2406 (2014).

[14] M. Lanza, "A review on resistive switching in high-k dielectrics: A nanoscale point of view using conductive atomic force microscope," Materials **7**(3), 2155–2182 (2014).

[15] H. Bae, B. C. Jang, H. Park, S. H. Jung, H. M. Lee, J. Y. Park, S. Jeon, G. Son, I. Tcho, K. Yu, S. U. Im, S. Choi, and Y. Choi, "Functional circuitry on commercial fabric via textile-compatible nanoscale film coating process for fibertronics," Nano Lett. **17**(10), 6443–6452 (2017).

[16] H. Du, C. L. Jia, A. Koehl, J. Barthel, R. Dittmann, R. Waser, and J. Mayer, "Nanosized conducting filaments formed by atomic-scale defects in redox-based resistive switching memories," Chem. Mater. **29**(7), 3164–3173 (2017).

[17] A. Zintler, U. Kunz, Y. Pivak, S. U. Sharath, S. Vogel, E. Hildebrandt, H.-J. Kleebe, L. Alff, and L. Molina-Luna, "FIB based fabrication of an operative Pt/HfO_2/TiN device for resistive switching inside a transmission electron microscope," Ultramicroscopy **181**, 144–149 (2017).

[18] K. H. Xue and X. S. Miao, "Oxygen vacancy chain and conductive filament formation in hafnia," J. Appl. Phys. **123**(16), 161505 (2018).

[19] C. Li, B. Gao, Y. Yao, X. Guan, X. Shen, Y. Wang, P. Huang, L. Liu, X. Liu, J. Li, C. Gu, J. Kang, and R. Yu, "Direct observations of nanofilament evolution in switching processes in HfO_2-based resistive random access memory by in situ TEM studies," Adv. Mater. **29**(10), 1602976 (2017).

[20] S. U. Sharath, S. Vogel, L. Molina-Luna, E. Hildebrandt, C. Wenger, J. Kurian, M. Duerrschnabel, T. Niermann, G. Niu, P. Calka, M. Lehmann, H. Kleebe, T. Schroeder, and L. Alff, "Control of switching modes and conductance quantization in oxygen engineered HfO_x based memristive devices," Adv. Funct. Mater. **27**(32), 1700432 (2017).

[21] M. P. Agustin, L. R. C. Fonseca, J. C. Hooker, and S. Stemmer, "Scanning transmission electron microscopy of gate stacks with HfO_2 dielectrics and TiN electrodes," Appl. Phys. Lett. **87**(12), 121909 (2005).

[22] E. Miranda, "Compact model for the major and minor hysteretic I–V loops in nonlinear memristive devices," IEEE Trans. Nanotechnol. **14**(5), 787–789 (2015).

[23] G. A. Patterson, J. Suñé, and E. Miranda, "Voltage-driven hysteresis model for resistive switching: SPICE modeling and circuit applications," IEEE Trans. Comput. Aided Des. Integrated Circuits Syst. **36**(12), 2044–2051 (2017).

[24]N. C. Saha and H. G. Tompkins, "Titanium nitride oxidation chemistry: An x-ray photoelectron spectroscopy study," J. Appl. Phys. **72**(7), 3072–3079 (1992).

[25]X. Guan, S. Yu, and H. S. P. Wong, "On the switching parameter variation of metal-oxide RRAM—Part I: Physical modeling and simulation methodology," IEEE Trans. Electron Devices **59**(4), 1172–1182 (2012).

[26]J. H. Weaver and H. P. R. Frederikse, *CRC Handbook of Chemistry and Physics* (CRC Press, Boca Raton, 1977), Vol. 76, pp. 12–156.

[27]B. Avasarala and P. Haldar, "Electrochemical oxidation behavior of titanium nitride based electrocatalysts under PEM fuel cell conditions," Electrochim. Acta **55**(28), 9024–9034 (2010).

[28]S. U. Sharath, M. J. Joseph, S. Vogel, E. Hildebrandt, P. Komissinskiy, J. Kurian, T. Schroeder, and L. Alff, "Impact of oxygen stoichiometry on electroforming and multiple switching modes in TiN/TaO$_x$/Pt based ReRAM," Appl. Phys. Lett. **109**(17), 173503 (2016).

[29]S. U. Sharath, T. Bertaud, J. Kurian, E. Hildebrandt, C. Walczyk, P. Calka, P. Zaumseil, M. Sowinska, D. Walczyk, A. Gloskovskii, T. Schroeder, and L. Alff, "Towards forming-free resistive switching in oxygen engineered HfO$_{2-x}$," Appl. Phys. Lett. **104**(6), 063502 (2014).

[30]D. J. Wouters, L. Zhang, A. Fantini, R. Degraeve, L. Goux, Y. Y. Chen, B. Govoreanu, G. Kar, G. Groeseneken, and M. Jurczak, "Analysis of complementary RRAM switching," IEEE Electron Device Lett. **33**(8), 1186–1188 (2012).

[31]J. J. Yang, D. B. Strukov, and D. R. Stewart, "Memristive devices for computing," Nat. Nanotechnol. **8**(1), 13 (2013).

[32]S. Kumar, C. E. Graves, J. P. Strachan, E. M. Grafals, A. L. D. Kilcoyne, T. Tyliszczak, J. Weker, J. Nishi, and R. S. Williams, "Direct observation of localized radial oxygen migration in functioning tantalum oxide memristors," Adv. Mater. **28**(14), 2772–2776 (2016).

[33]E. Linn, R. Rosezin, C. Kügeler, and R. Waser, "Complementary resistive switches for passive nanocrossbar memories," Nat. Mater. **9**(5), 403 (2010).